Efficient Numerical Computation and Experimental Study of Temporally Long Equilibrium Scour Development around Abutment

JAAN HUI PU, Assistant Professor, *53, Kabanbay Batyr Avenue, School of Engineering, Nazarbayev University, Astana 010000, Republic of Kazakhstan.*
Email: jhpu@nu.edu.kz (author of correspondence)

SIOW YONG LIM, Associate Professor, *School of Civil and Environmental Engineering, Nanyang Technological University, Singapore 639798.*
Email: CSYLIM@ntu.edu.sg

ABSTRACT

For the abutment bed scour to reach its equilibrium state, a long flow time is needed. Hence, the employment of usual strategy of simulating such scouring event using the 3D numerical model is very time consuming and less practical. In order to develop an applicable model to consider temporally long abutment scouring process, this study modifies the common approach of 2D shallow water equations (SWEs) model to account for the sediment transport and turbulence, and provides a realistic approach to simulate the long scouring process to reach the full scour equilibrium. Due to the high demand of the 2D SWEs numerical scheme performance to simulate the abutment bed scouring, a recently proposed surface gradient upwind method (SGUM) was also used to improve the simulation of the numerical source terms. The abutment scour experiments of this study were conducted using the facility of Hydraulics Laboratory at Nanyang Technological University, Singapore to compare with the presented 2D SGUM-SWEs model. Fifteen experiments were conducted over a total period of 3059.7 hours experimental time (over 4.2 months). The comparison shows that the 2D SGUM-SWEs model gives good representation to the experimental results with the practical advantage.

Keywords: Abutment; equilibrium scour; experiment; numerical computation; SGUM model; SWEs model; time development

1 Introduction

In the progress of the abutment structure scouring flow studies, various numerical and experimental models have been proposed in literature [1,2]. The review by Ettema et al. [3]

outlined the uncertainties involved in the abutment scour measurement and physical modelling, and highlighted the importance of accurate estimation of the abutment scour.

In the experimental studies developed, the emphasis has been put on the time development of the scour to reach the equilibrium state due to the overwhelming fact that this time development carries the essential information of the abutment stability study [4,5,6]. As suggested by Dey and Barbhuiya [4], long duration experiment is tedious and time consuming to be performed, and there was a lack of good data sets about the required period to reach the equilibrium scouring conditions. Lim's [7] abutment scour experiments revealed that very long duration is needed to reach the equilibrium scour state (up to 3 to 8 days, depending on the flow and bed sediment conditions). Similar conclusion of long scouring equilibrium period has also been drawn for bridge pier scour study by Lu et al. [8] who used 2-4 days for their experimental scour development. To this end, both the experimental and numerical approaches in this study are designed for exploring and investigating abutment scour development in a floodplain for long scouring period up to its equilibrium condition. The experiments were conducted for about 2 to 23 days depending on the abutment size and flow conditions [9], whereas the numerical modelling was constructed by modifying the finite volume (FV) model of Pu's [10] work.

The previous numerical modelling studies suggested that the 3D Navier Stokes (NS)-type model could accurately capture the abutment scouring [11,12], but costly meshing or numerical advancements are usually involved, which contributes additional computational burden to the readily high computational cost of the 3D model. Several numerical comparisons have been conducted between 3D NS and 2D shallow water equations (SWEs) models on different flow conditions at experiments or field studied cases [13,14]. They summarised that compared the accuracy provided by the 3D NS model and the efficiency presented by the 2D SWEs model, the latter is a better choice in their respective investigated cases. A more comprehensive error analysis of the 2D SWEs model as compared to the 3D NS model has been recently conducted by Mahdizadeh et al. [15], in which same conclusion was drawn that the 2D SWEs simulations satisfactorily represented the turbulence flow wave applications with much better efficiency.

After considering the literature studies, the 2D SWEs model has shown to be a tangible solution to estimate the long equilibrium scouring process; hence it was used in this study. The model shows great success in representing a wide range of complicated sediment transport and fluvial processes, such as presented in the studies of Cao et al. [16], Wu and Wang [17,18], Xia et al. [19], and Cao and Pender [20]. For the employed SWEs model to simulate the turbulence abutment bed scouring, the sediment transport continuity-concentration (SCC) model was used by adapting the non-capacity concept used in Cao et al. [16] and Cao and Pender [20]; whereas the

flow turbulence was simulated by a standard 2D k-ε model used in Younus and Chaudhry [21] and Cea et al. [22]. The full model of this study was constructed by the fully coupled concept, and it was based on the finite volume (FV) method. Numerically, the monotonic upwind scheme of conservative laws (MUSCL)-Hancock scheme was used with the Harten Lax van Leer-contact (HLLC) approximate Riemann solver to discretize the FV model. The source terms of the numerical scheme was treated using a surface gradient upwind method (SGUM) originally proposed by Pu et al. [23]. This method integrates the source term treatment into the inviscid discretization scheme using the upwind approach, and thus to enhance the simulation stability and accuracy for the heavily source terms affected bed scouring flow in this study.

The comparison of our laboratory measurements and numerical simulations showed that the improved 2D SWEs model has demonstrated a good trend to capture the temporal scouring around abutment with good agreement up to the equilibrium scouring state. The comparison also showed that the simulated scour map was produced with good resemblance to the measurements, and it proved the predictive nature of the presented SGUM-SWEs model to reproduce the whole equilibrium scouring process without expensive numerical cost.

2 Numerical Models

2.1 *Shallow water equations (SWEs) model*

In this study, the SWEs model is used to couple with the k-ε and SCC models. The 2D fully conservative shallow water equations are presented in equations (1) – (3), and it is combined with the terms from the SCC model as suggested by Cao et al. [16] and Cao and Pender [20], and the terms from the k-ε model as proposed by Younus and Chaudhry [21].

$$\frac{\partial \phi}{\partial t}+\frac{\partial \phi u}{\partial x}+\frac{\partial \phi v}{\partial y}=\frac{g}{1-\lambda}\left(e_{sc}-d_{sc}\right) \tag{1}$$

$$\begin{aligned}&\frac{\partial \phi u}{\partial t}+\frac{\partial\left(\phi u^{2}+\phi^{2}/2\right)}{\partial x}+\frac{\partial \phi uv}{\partial y}-\frac{\partial}{\partial x}\left[2\nu_{t}\frac{\partial\left(\phi u\right)}{\partial x}-\frac{2}{3}\phi k\right]-\frac{\partial}{\partial y}\left[\nu_{t}\left[\frac{\partial\left(\phi u\right)}{\partial y}+\frac{\partial\left(\phi v\right)}{\partial x}\right]\right]\\&=g\phi\left(S_{ox}-S_{fx}\right)-\frac{\phi^{2}\left(\rho_{s}-\rho_{w}\right)}{2\rho}\frac{\partial C}{\partial x}+\frac{ug\left(\rho_{o}-\rho\right)\left(d_{sc}-e_{sc}\right)}{\rho\left(1-\lambda\right)}\end{aligned} \tag{2}$$

$$\begin{aligned}&\frac{\partial \phi v}{\partial t}+\frac{\partial \phi uv}{\partial x}+\frac{\partial\left(\phi v^{2}+\phi^{2}/2\right)}{\partial y}-\frac{\partial}{\partial x}\left[\nu_{t}\left[\frac{\partial\left(\phi u\right)}{\partial y}+\frac{\partial\left(\phi v\right)}{\partial x}\right]\right]-\frac{\partial}{\partial y}\left[2\nu_{t}\frac{\partial\left(\phi v\right)}{\partial y}-\frac{2}{3}\phi k\right]\\&=g\phi\left(S_{oy}-S_{fy}\right)-\frac{\phi^{2}\left(\rho_{s}-\rho_{w}\right)}{2\rho}\frac{\partial C}{\partial y}+\frac{vg\left(\rho_{o}-\rho\right)\left(d_{sc}-e_{sc}\right)}{\rho\left(1-\lambda\right)}\end{aligned} \tag{3}$$

In equations (1) – (3), the variable ϕ refers to geopotential, and is given by $\phi = g \cdot h$; where h is the water depth; g is the gravitational acceleration. u and v are the depth averaged flow velocities in streamwise and lateral directions, respectively; ρ_s and ρ_w are density of sediment and water, respectively; in which, $\rho = \rho_w(1-C) + \rho_s C$; $\rho_o = \lambda\rho_w + (1-\lambda)\rho_s$; C is the flux averaged volumetric sediment concentration; λ is the sediment bed porosity; and e_{sc} and d_{sc} are sediment erosion and deposition rates, respectively. k is the flow energy, and the depth averaged turbulent viscosity ν_t is calculated as $\nu_t = C_\mu k^2/\varepsilon$, where $C_\mu = 0.09$. x, y and t denote the spatial-longitudinal, spatial-transverse and temporal domains, respectively.

In the flow applications with erodible bed, an additional source term is implemented into the right hand side of equation (1) to capture the influence of the erosion rate e_{sc} and deposition rate d_{sc} to water flow, where this term represents the mass conservation of water-sediment mixture. The second and third terms on the right hand side of equations (2) and (3) represent the spatial variations of sediment concentration and momentum transfer due to the process of sediment exchange between the water flow and erodible bed. Ferreirra and Leal [24], Yang and Greimann [25], Brufau et al. [26] and more recently Xia et al. [19] had suggested that the effects of these two terms in equations (2) and (3) are insignificant in most flow applications.

In equations (2) and (3), S_{ox} and S_{oy} are the bed slopes in the streamwise and lateral directions, respectively. The friction slope of the channel S_f in the same equations are given by

$$S_{fx} = \frac{n^2 u\sqrt{u^2+v^2}}{h^{4/3}}, \text{ and } S_{fy} = \frac{n^2 v\sqrt{u^2+v^2}}{h^{4/3}} \tag{4}$$

where n is the Manning's friction coefficient.

2.2 *Turbulence model*

The k-ε equations are coupled with the SWEs model to represent the flow turbulence. The equations can be presented as [21,22]

$$\frac{\partial \phi k}{\partial t} + \frac{\partial \phi u k}{\partial x} + \frac{\partial \phi v k}{\partial y} - \frac{\partial}{\partial x}\left(\frac{\nu_t}{\sigma_k}\cdot\frac{\partial(\phi k)}{\partial x}\right) - \frac{\partial}{\partial y}\left(\frac{\nu_t}{\sigma_k}\cdot\frac{\partial(\phi k)}{\partial y}\right) = g\cdot R_h + g\cdot R_k - \phi\varepsilon \tag{5}$$

$$\frac{\partial \phi \varepsilon}{\partial t} + \frac{\partial \phi u \varepsilon}{\partial x} + \frac{\partial \phi v \varepsilon}{\partial y} - \frac{\partial}{\partial x}\left(\frac{\nu_t}{\sigma_\varepsilon}\cdot\frac{\partial(\phi\varepsilon)}{\partial x}\right) - \frac{\partial}{\partial y}\left(\frac{\nu_t}{\sigma_\varepsilon}\cdot\frac{\partial(\phi\varepsilon)}{\partial y}\right) = \frac{\varepsilon}{k}\left(g\cdot C_1\cdot R_h - C_2\cdot\phi\varepsilon\right) + g\cdot R_\varepsilon \tag{6}$$

where ε is the flow energy dissipation. Each of the parameter, R_h, R_k, and R_ε in equations (5) and (6) can be represented as

$$R_h = \frac{\nu_t}{z}\left\{2\left[\frac{\partial(hu)}{\partial x}\right]^2 + 2\left[\frac{\partial(hv)}{\partial y}\right]^2 + \left[\frac{\partial(hu)}{\partial y} + \frac{\partial(hv)}{\partial x}\right]^2\right\}, R_k = \frac{n^2 g}{h^{\frac{1}{3}}}\left(u^2+v^2\right)^{\frac{3}{2}}, \text{ and}$$

$$R_\varepsilon = \frac{C_2 C_\mu n^{\frac{5}{2}} g^{\frac{5}{4}}\left(u^2+v^2\right)^2}{hD^{\frac{1}{2}}h^{\frac{5}{12}}} \tag{7}$$

Standard values are used for the turbulence parameters in equations (5) to (7) and they are given as $C_1 = 1.44$, $C_2 = 1.92$, $\sigma_k = 1.0$, $\sigma_\varepsilon = 1.3$, and $D = 1.0$.

2.3 *Sediment transport model*

The SCC equations are employed to represent the impact of sediment transport, and these equations could be represented as [16,20]

$$\frac{\partial \phi C}{\partial t} + \frac{\partial \phi C u}{\partial x} + \frac{\partial \phi C v}{\partial y} = g\left(e_{sc} - d_{sc}\right) \tag{8}$$

$$\frac{\partial z_b}{\partial t} = \frac{1}{1-\lambda}\cdot\left(d_{sc} - e_{sc}\right) \tag{9}$$

where z_b is the mobile bed elevation. The sediment erosion and deposition rates, e_{sc} and d_{sc}, are used in the source terms on the right hand side of equations (1), (8) and (9). Their evaluations hold a dominant role to determine the flow transport characteristics, and their simulations were achieved in this study by using the SGUM.

In sediment transport modelling studies, different relationships have been suggested to determine e_{sc} and d_{sc}, such as the studies by Cao et al. [16], Xia et al. [19], Zhou and Lin [27] and Valiani and Caleffi [28]. Among these studies, the relationships of e_{sc} and d_{sc} suggested by Zhou and Lin [27] and Valiani and Caleffi [28] have exhibited great success in a wide range of tests and applications due to: (1) their consideration of multiple sediment transport parameters into the determination of e_{sc} and d_{sc}, and (2) their usage of empirically calibrated constants have been kept to a minimum. According to the suggestion of Zhou and Lin [27] and Valiani and Caleffi [28], we will have

$$d_{sc} - e_{sc} = \frac{w_V\left(C - C_E\right)}{l_A} \tag{10}$$

where w_V is the sediment fall velocity, C_E is the equilibrium sediment concentration, and l_A is the dimensionless adaptation length scale for sediment; and Valiani and Caleffi [28] further suggested that C_E could be represented as

$$C_E = A\left[\frac{u^2+v^2}{(s_s-1)gd_d}\right]^B \tag{11}$$

in which, A and B are coefficients for the equilibrium concentration; s_s is the specific density of the sediment; and d_d is the sediment median diameter.

The dimensionless adaptation length scale for the sediment l_A used in equation (10) can be represented using an empirical formula utilised in Valiani and Caleffi [28] and Armanini and Di Silvio [29] as presented in equation (12).

$$l_A = \frac{l_R}{h} + \left(1-\frac{l_R}{h}\right)\cdot\exp\left[-1.5\left(\frac{l_R}{h}\right)^{-1/6}\frac{w_V}{u_s}\right] \tag{12}$$

For the variables in equation (12), u_s is the shear velocity of the flow; and l_R is a reference level used as a comparison with the flow depth. l_R is usually assumed to be of the same order of magnitude as the hydraulic roughness. In this study, $l_R = 2d_d$ is used, as suggested by Valiani and Caleffi [28].

2.4 *Numerical scheme*

In this study, the numerical flux term was discretized using a Godunov-type Hancock scheme. This scheme was upgraded by a two-stage predictor-corrector time-stepping concept. The Harten Lax van Leer-contact (HLLC) approximate Riemann solver was used to couple with the Godunov-type Hancock scheme for the Riemann data reconstruction process. The slope limiter method was used in the HLLC solver to ensure the space discretization scheme satisfying the flux-limiting property. The source term of the proposed numerical scheme was modelled by a surface gradient upwind method (SGUM) as proposed by Pu et al. [23].

By defining equations (1) – (3), (5) – (6) and (8) – (9) into a single vector operation, we will get

$$\frac{\partial \mathbf{U}}{\partial t} + \nabla\cdot\mathbf{F} = \mathbf{S} \tag{13}$$

where

$$\mathbf{U}=\begin{bmatrix}\phi\\ \phi u\\ \phi v\\ \phi k\\ \phi\varepsilon\\ \phi C\\ z_b\end{bmatrix},\ \mathbf{F}=\begin{bmatrix}\phi Q\\ \phi uQ+\dfrac{\phi}{2}\left(\phi+\dfrac{4}{3}k\right)-2\nu_t\cdot\left(\nabla_x\cdot\left(\phi Q\right)+\nabla_y\cdot\left(\dfrac{\phi u}{2}\right)\right)\\ \phi vQ+\dfrac{\phi}{2}\left(\phi+\dfrac{4}{3}k\right)-2\nu_t\cdot\left(\nabla_y\cdot\left(\phi Q\right)+\nabla_x\cdot\left(\dfrac{\phi v}{2}\right)\right)\\ \dfrac{\nu_t}{\sigma_k}\cdot\nabla\cdot\left(\phi k\right)\\ \dfrac{\nu_t}{\sigma_\varepsilon}\cdot\nabla\cdot\left(\phi\varepsilon\right)\\ \phi CQ\\ 0\end{bmatrix},\ \text{and,}$$

$$\mathbf{S}=\begin{bmatrix}\dfrac{g}{1-\lambda}\left(e_s-d_s\right)\\ g\phi\left(S_{ox}-S_{fx}\right)-\dfrac{\phi^2\left(\rho_s-\rho_w\right)}{2\rho}\dfrac{\partial C}{\partial x}+\dfrac{ug\left(\rho_o-\rho\right)\left(d_s-e_s\right)}{\rho\left(1-\lambda\right)}\\ g\phi\left(S_{oy}-S_{fy}\right)-\dfrac{\phi^2\left(\rho_s-\rho_w\right)}{2\rho}\dfrac{\partial C}{\partial y}+\dfrac{vg\left(\rho_o-\rho\right)\left(d_s-e_s\right)}{\rho\left(1-\lambda\right)}\\ g\cdot P_h+g\cdot P_k-\phi\varepsilon\\ \dfrac{\varepsilon}{k}\left(g\cdot C_1\cdot P_h-C_2\cdot\phi\varepsilon\right)+g\cdot P_\varepsilon\\ g\left(e_s-d_s\right)\\ \dfrac{1}{\left(1-\lambda\right)}\left(d_s-e_s\right)\end{bmatrix}\qquad(14)$$

In equations (13) and (14), $\mathbf{U}$, $\mathbf{F}$ and $\mathbf{S}$ represent vector forms for the flow conserved variables, numerical flux and source terms, respectively; Q is the resultant velocity defined by $Q=\sqrt{u^2+v^2}$; and ∇ is the gradient operator that can be expressed by $\nabla=\nabla_x+\nabla_y$, where $\nabla_x=\mathbf{i}\cdot\partial/\partial x$ and $\nabla_y=\mathbf{j}\cdot\partial/\partial y$. $\mathbf{i}$ and $\mathbf{j}$ are the unit vectors in streamwise and lateral directions, respectively.

3.1 *Harten Lax van Leer-Contact (HLLC) Approximate Riemann Solver*

In this study, the HLLC approximate Riemann solver used was suggested in Toro [30] and has been further tested in Hu et al. [31]. The HLLC numerical flux is determined by

$$\mathbf{F}^{hllc} = \begin{cases} \mathbf{F}_L & \text{for} \quad 0 \le s_L \\ \mathbf{F}_L^* = \mathbf{F}_L + s_L\left(\mathbf{U}_L^* - \mathbf{U}_L\right) & \text{for} \quad s_L \le 0 \le s_* \\ \mathbf{F}_R^* = \mathbf{F}_R + s_R\left(\mathbf{U}_R^* - \mathbf{U}_R\right) & \text{for} \quad s_* \le 0 \le s_R \\ \mathbf{F}_R & \text{for} \quad s_R \le 0 \end{cases} \tag{15}$$

and

$$\mathbf{U}_D^* = \left(\frac{s_D - u_D}{s_D - s_*}\right)\mathbf{U}^* \tag{16}$$

Subscripts L and R represent the left and right regions of a solution computational cell, respectively; and superscript * represents the star region that separates the left and right regions. In HLLC solver, a wave speed s_* is employed in the star region for updating the numerical flux. The subscript D in equation (16) represents the direction of the parameters (left L or right R). The wave speeds in equations (15) and (16) are given by:

$$\begin{aligned} s_L &= \min\left[u_L - c_L,\ u_* - c_*\right] \\ s_* &= \frac{\left(u_L + u_R\right)}{2} + c_L - c_R = u_* \\ s_R &= \min\left[u_R + c_R,\ u_* + c_*\right] \end{aligned} \tag{17}$$

where c is the wave celerity ($c = \sqrt{gh}$), and at the * region, c^* is estimated as

$$c^* = \frac{\left(c_L + c_R\right)}{2} + \frac{\left(u_L - u_R\right)}{4} \tag{18}$$

In the shock capturing process as utilised by the HLLC solver, the "dry" water wave front has to be resolved before obtaining a stable algorithm. In this study, further criteria as suggested by Toro [30] are included to handle the water wave front condition on the left and right "dry" sides as follows

Left "Dry" Side Criteria: $s_L = u_R - 2c_R$, $s_* = s_L$, and $s_R = u_R + c_R$ (19)

Right "Dry" Side Criteria: $s_R = u_L + 2c_L$, $s_* = s_R$, and $s_L = u_L - c_L$ (20)

3.2 *Monotone Upwind–Hancock Scheme*

In this study, a robust numerical wave reconstruction scheme, Monotone Upwind Scheme for Conservative Laws (MUSCL), was used, in which both $\mathbf{U}_L$ and $\mathbf{U}_R$ are updated linearly according to their adjacent cells [30]. The MUSCL scheme gives a second order of accuracy to the proposed FV model, and it can be expressed as

$$\mathbf{U}_{i+1/2}^{L} = \mathbf{U}_{i} - \frac{\prod(q_i)\cdot\Delta\mathbf{U}_{i-1/2}}{2}, \text{ and, } \mathbf{U}_{i+1/2}^{R} = \mathbf{U}_{i+1} + \frac{\prod(q_{i+1})\cdot\Delta\mathbf{U}_{i+1/2}}{2} \tag{21}$$

$$\text{where } q_i = \frac{\Delta\mathbf{U}_{i+1/2}}{\Delta\mathbf{U}_{i-1/2}},\ q_{i+1} = \frac{\Delta\mathbf{U}_{i+3/2}}{\Delta\mathbf{U}_{i+1/2}},\ \Delta\mathbf{U}_{i+1/2} = \mathbf{U}_{i+1} - \mathbf{U}_{i}, \text{ and, } \Delta\mathbf{U}_{i-1/2} = \mathbf{U}_{i} - \mathbf{U}_{i-1} \tag{22}$$

$\prod$ is the slope limiter in equations (21) – (22); i represents the space step; and q is the gradient of successive $\Delta\mathbf{U}$. As suggested by the findings from Hu et al. [31] and Mingham and Causon [32], the MUSCL scheme flux in this study is determined using the van Leer slope limiter, where $\prod = \left[q + |q|\right] / (1+q)$.

A Hancock two-stage predictor-corrector scheme was utilised to update $\mathbf{U}$ across the time domain. This approach has the advantage of being stable and could achieve second order accuracy over the time domain. The predictor-corrector steps are given as

$$\textit{Predictor Step}:\ \mathbf{U}_{i}^{N+1/2} = \mathbf{U}_{i}^{N} - \frac{\Delta t}{2\Omega_i}\left(\mathbf{F}_{i+1/2}^{N} - \mathbf{F}_{i-1/2}^{N}\right) \tag{23}$$

$$\textit{Corrector Step}:\ \mathbf{U}_{i}^{N+1} = \mathbf{U}_{i}^{N} - \frac{\Delta t}{\Omega_i}\left(\mathbf{F}_{i+1/2}^{N+1/2} - \mathbf{F}_{i-1/2}^{N+1/2}\right) \tag{24}$$

where Ω is the cell area (for the SWEs model); and N represents the time step.

The Courant-Friedrichs-Lewy stability criterion was used to ensure Δt does not exceed its maximum allowable limit, as represented by

$$\Delta t \le C_{FL}\left[\frac{\Omega}{|Q\cdot\mathbf{s}| + c\cdot|\mathbf{s}|}\right] \tag{25}$$

where $\mathbf{s} = \mathbf{i} + \mathbf{j}$ represents the resultant normal unit vector; and C_{FL} is the Courant number, which is limited to $0 < C_{FL} \le 1$. Smaller values of C_{FL} will give more accurate and stable results, but at an increasing computational expense.

3.3 *Source Terms Scheme*

A surface gradient upwind method (SGUM) for the numerical source terms treatment proposed by Pu et al. [23] was integrated into this study to describe the combined operation of $\mathbf{F}$ and $\mathbf{S}$ in equation (13). The combination of $\mathbf{F}$ and $\mathbf{S}$ in the numerical iterations used in the SGUM could improve the numerical accuracy to predict the flow under different sediment transport conditions (including the investigated abutment bed scouring), since these conditions are heavily source terms bonded. Besides improving the source terms simulation from the SCC equations, the

SGUM can also improve the simulation of extra source terms generated from the k-ε equations into the SWEs model.

It is worth mentioning that in Pu et al. [23], the SGUM was only applied to the 1D water flow cases, but here it is used for the 2D SWEs model with sediment transport. With the application of SGUM, the MUSCL-Hancock scheme in equations (23) – (24) will become

$$\textit{Predictor Step}:\ \mathbf{U}_i^{N+1/2} = \mathbf{U}_i^N - \frac{\Delta t}{2\Omega_i}\left(\mathbf{f}_{i+1/2}^N - \mathbf{f}_{i-1/2}^N\right) \tag{26}$$

$$\textit{Corrector Step}:\ \mathbf{U}_i^{N+1} = \mathbf{U}_i^N - \frac{\Delta t}{\Omega_i}\left(\mathbf{f}_{i+1/2}^{N+1/2} - \mathbf{f}_{i-1/2}^{N+1/2}\right) \tag{27}$$

where $\mathbf{f} = \mathbf{F} - \Omega \cdot \mathbf{S}$.

Similar representations of the Hancock scheme in equations (26) and (27) have also been used by Hu et al. [31], Mingham and Causon [32], Sanders et al. [33] and many others in their 2D SWEs schemes with or without considering the sediment transport, except that the source terms here have been integrated into the Hancock scheme by using $\mathbf{f}$ as presented above.

3.4 *Boundary and Initial Conditions*

A double boundary condition is used for the proposed model, where two extra ghost-cells are utilised outside the computational space domain [31]. Two kinds of boundary are considered, the open and solid boundaries. For their corresponding boundary vectors $\boldsymbol{U}^B$, it can be presented as

$$\textit{Solid Boundary}:\ \boldsymbol{U}^B = \left[\phi \quad \phi u \quad \phi v \quad \phi k \quad \phi\varepsilon\right]^T \tag{28}$$

$$\textit{Transmissive Boundary}:\ \boldsymbol{U}^B = \left[\phi \quad -\phi u \quad -\phi v \quad \phi k \quad \phi\varepsilon\right]^T \tag{29}$$

These boundary conditions are updated by using

$$\mathbf{U}_{m+1}^B = \mathbf{U}_m^B \tag{30}$$

$$\mathbf{U}_{m+2}^B = \mathbf{U}_{m-1}^B \tag{31}$$

where m is the last space step in the computational boundary excluding the ghost cells.

3 Physical Model

3.1 *Experiment Descriptions*

The experiments of our study were conducted in an asymmetrical 19-m long two-stage channel located at the Hydraulics Laboratory of the Nanyang Technological University, Singapore [9,34]. The channel width is 1.6 m, where the floodplain is 1 m wide and the main channel is 0.6 m wide,

and it has a longitudinal bed slope of 0.00116. A 2.5 m long and 0.4 m deep (floodplain) sand recess section is installed at 11 m downstream from the flume entrance. For 2 m length upstream of the sand recess, the floodplain bed is coated with the same kind of sand. A tailgate is used at the downstream end of the channel to adjust the water level in the channel. The header tank is equipped with perforated steel plates and sponge layer to reduce turbulence and water surface undulation and to provide uniform water distribution to the channel. The inflow discharge was measured using a magnetic flow meter which can measure up to an accuracy of 1 m^3/hr, and its speed is controlled using a frequency inverter controller. Velocity profiles at the approaching section, at 11 m from the channel entrance, were measured using a 3-D acoustic Doppler velocimeter (ADV) to calculate the component discharges in the floodplain and the main channel [34]. The water level was measured at the approaching flow section, and also along the channel to obtain the overall water surface elevation to an accuracy of ± 2 mm.

The sand used in the experiment has a median size of $d_d = d_{50} = 0.9$ mm and a geometric standard deviation $\sigma_g = d_{84} / d_{50}$ of 1.05. The box-like abutment used in the experiments consists of three lengths 20cm, 35cm and 50cm with constant width of 5cm. All the tests were conducted with a single abutment installed perpendicularly to the channel sidewall at 1 m location after the upstream edge of the sand recess, i.e. at 12 m from the channel entrance. The scour depth was measured using a periscope which can be inserted into the 5 cm thick box-like abutment all the way to the bottom of the sand bed. The position of the scoured bed surface was observed from the periscope and the time development of scour depth at the abutment nose can be measured to an accuracy of ±1 mm.

For a typical test, the tailgate was first set at a sufficiently high level while the flume was slowly filled with water. Then the discharge was gradually raised up to the designated value while the tailgate was gradually adjusted to the position which gave the desired flow depth for the given discharge. The scour depth development was monitored and recorded for different time interval according to the scouring rate until there is no noticeable sand movement around the deepest part of the scour hole. Fig. 1 shows the schematic and photographic examples of the scour hole after it reached the equilibrium condition.

For the hydraulic conditions tested herein, the scouring duration varies from 46 to 546 hours, where some had also run for longer period to ensure that the equilibrium scouring condition was reached. The flow discharges as well as the flow depth ratios were varied for the three abutment lengths tested. Table 1 shows the details of the hydraulic conditions, scouring duration (actual flow time) and equilibrium scour period for the 15 test runs conducted. Each test was given a

code, say Run 20-60-02. The first number refers to the abutment length, i.e., $L = 20$ cm, the second number is the discharge from the magnetic flow meter $Q_{fm} = 60$ l/s and the last number is the flow depth ratio $d_f / d_m = 0.2$, where d_f is the flow depth in the floodplain and d_m in the flow depth in the main channel.

3.2 *Determination of Equilibrium Scouring Duration*

In this study, the equilibrium scouring time t_e is defined as the time when the increase of scour depth is less than or equal to 1 mm for an observation interval of 6 to 12 hours. In cases where fluctuation of scour depth was observed near the equilibrium condition, the equilibrium time is defined as the time when the maximum scour depth was first recorded in the scour-time curve before the fluctuations of scour depth begins. As an example, Fig. 2 shows the scour-time curves for three runs with the same discharge obtained from the integration of ADV point-measured velocities $Q_{vel} = 48$ l/s, and the same flow depth ratio $d_f / d_m = 0.3$, but with different abutment lengths: $L = 20$ cm, 35 cm and 50 cm. The figure hints that the equilibrium time is challenging to be determined as the difference in the scour depths near the equilibrium conditions are quite small. Due to this reason, the very long scouring duration is needed to ensure the reaching of equilibrium scouring state in a flow.

4 Results and Discussions

In this section, the comparisons between our experimental results and numerical computations are presented and discussed. Using the equilibrium scouring time t_e and its corresponding equilibrium scour depth d_{se}, the plots of normalised scour depth d_s / d_{se} versus normalised time t / t_e are produced in Figs. 3 to 5, where d_s is the scour depth at any particular flow time t. The figures show that the scour-time curves are of the exponential-type function which is typical for pier and abutment scour [35,36]. Based on these figures, it can also be observed that the scour increases very rapidly in the early stage, where about 80% of d_s / d_{se} could be reached in 20% of t / t_e. However from the figures we can also observe that the last 20% of d_s / d_{se} is lasted in a long tail that occupied 80% of t / t_e towards the scouring equilibrium $t = t_e$. Hence, short term scour data from some published literature should be examined cautiously as to whether the equilibrium scouring criteria can be met.

For the comparison of the numerical computations and the experimental measurements of the 20 cm abutment test in Fig. 3, the proposed numerical model simulates the measured data with good agreement. However, the relatively small mismatches are observed at the beginning of the scouring in Fig. 3. Similar mismatches are also observed at the beginning of the tests with 35 cm and 50 cm abutments. These mismatches are believed to be caused by the initial scouring condition that has been heavily influenced by the secondary currents and corner flows, in which those flow events have not been considered in the presented numerical model. As expected, these mismatches are becoming lesser as t/t_e increases. In Figs. 4 and 5, the comparisons of the d_s/d_{se} profiles also show good correspondence between the numerical simulations and experimental results for the flow tests with 35cm and 50cm abutments, respectively. In comparison, Fig. 5 presents the best agreement between the proposed numerical simulations and measured data.

Fig. 6 presents the scouring map comparison between the numerical simulation and the measured scoured bed contours for the experimental run 20-70-04. The figure reveals that the 2D SGUM-SWEs simulation can well-capture the bed contours of the complicated scour hole at the heaviest scoured region behind the abutment. The most obvious difference of the numerical prediction and measurements occurs at the abutment boundary, where the corner flows are expected to be significant compared to all the other locations. Fig. 6 shows convincingly that the proposed 2D SGUM-SWEs model can be employed as a reasonable tool for simulating the abutment scouring flow application, due to its much lower computational cost than the 3D flow models. Moreover, due to the fact that the physical equilibrium abutment scour is usually a very time-consuming process, the SWEs-type approach should be given serious consideration for obvious practical reason.

5 Conclusions

In this study, a proposed fully coupled 2D shallow water numerical model was used to represent the physical abutment scouring process until the equilibrium scour condition was reached. The proposed numerical model considers all water flow continuity and momentum conditions, flow turbulence and sediment transport using the shallow water equations (SWEs), k-ε and sediment continuity-concentration (SCC) models, respectively. A numerical well-balanced surface gradient upwind method (SGUM) was implemented to improve the source terms simulation of the combined SWEs model. Besides the numerical works, fifteen temporally long physical experiments were also conducted using the facility of Hydraulic Laboratory at Nanyang

Technological University, Singapore over the period of 46 to 546 hours to investigate the abutment scour up to the equilibrium scouring state.

Compared the numerical predictions and experimental results, we can conclude that the proposed SGUM-SWEs model could well simulate the abutment scour until the equilibrium scouring state was reached. At the initial scouring, the SGUM-SWEs simulations were found to slightly depart from the measured data. This observed outcome was due to the amplified scouring by the secondary currents and corner flows in the laboratory condition that has not been considered in the SGUM-SWEs model. The comparison of the numerical simulated and laboratory measured scouring map at the Run 20-70-04 further showed that the SGUM-SWEs model is capable to reproduce the complicated abutment scouring measurements with good agreement. The finding of this study shows that the 2D SWEs-type model is a tangible solution to represent the equilibrium abutment scouring.

Acknowledgements

The first and corresponding author Dr Jaan Hui Pu acknowledges the support of the Nazarbayev University Seed Grant project entitled "Environmental Assessment of Sediment Pollution Impact on Hydropower Plants". The authors would like to thank Dr Joko Nugroho for providing his PhD experimental data (under the supervision of the second author Dr Siow Yong Lim).

Nomenclatures

c	wave celerity
C	flux averaged volumetric sediment concentration
C_E	equilibrium sediment concentration
C_{FL}	Courant number
d_d	sediment median diameter
d_f	flow depth in floodplain
d_m	flow depth in main channel
d_s	scour depth
d_{sc}	sediment deposition rate
d_{se}	equilibrium scouring depth
e_{sc}	sediment erosion rate
g	gravitational acceleration
h	water depth
i	space step

k	flow energy
L	abutment length
l_A	dimensionless adaptation length scale
m	last time space
n	Manning's friction coefficient
N	time step
Q	resultant velocity
Q_{fm}	discharge from magnetic flow meter
Q_{vel}	discharge obtained from integration of ADV point-measured velocities
s	wave speed
S_f	friction/energy slope of flow
S_o	bed slope
s_s	sediment specific density
t	time domain
t_{actual}	actual scouring time run for an experiment
t_e	equilibrium scouring time
u	depth averaged flow velocity in streamwise direction
U_f	flow velocity at flood plain
U_m	flow velocity at main channel
u_s	shear velocity
v	depth averaged flow velocity in lateral direction
w_v	sediment fall velocity
x	spatial-longitudinal domain
y	spatial-transverse domain
z_b	mobile bed elevation
∇	gradient operator
ε	flow energy dissipation
λ	sediment bed porosity
ν_t	depth averaged turbulent viscosity
Ω	computational cell area
ϕ	flow geopotential
Π	slope limiter
ρ_s	density of sediment

ρ_w density of water

σ_g geometric standard deviation of sediment size

Subscripts and Symbols

ADV acoustic Doppler velocimeter

FV finite volume

HLLC Harten Lax van Leer-contact

L left region

MUSCL monotonic upwind scheme for conservative laws

NS Navier Stokes

R right region

SCC sediment transport continuity-concentration

SGUM surface gradient upwind method

SWEs shallow water equations

* star region

References

[1] Yin J, Chen Y, Falconer RA (2003) Steady Shallow-Water Current and Solute Transport around a Semi-Conical Headland. Environ Fluid Mech 3(3):221-234

[2] Souhar O, Faure J-B, Paquier A (2007) Automatic Sensitivity Analysis of a Finite Volume Model for Two-Dimensional Shallow Water Flows. Environ Fluid Mech 7(4):303-315

[3] Ettema R, Yoon B, Nakato T, Muste M (2004) A Review of Scour Conditions and Scour-Estimation Difficulties for Bridge Abutments. KSCE J Civil Eng 8(6):643-650

[4] Dey S, Barbhuiya AK (2005) Time Variation of Scour at Abutments. J Hydraulic Eng 131(1):11-23

[5] Yanmaz AM, Kose O (2007) Time-wise Variation of Scouring at Bridge Abutments. Sādhanā 32(3):199-213

[6] Ballio F, Radice A, Dey S (2010) Temporal Scales for Live-Bed Scour at Abutments. J Hydraulic Eng 136(7):395-402

[7] Lim SY (1997) Equilibrium Clear-Water Scour around an Abutment. J Hydraulic Eng 123(3):237-243

[8] Lu J-Y, Shi Z-Z, Hong J-H, Lee J-J, Raikar RV (2011) Temporal Variation of Scour Depth at Nonuniform Cylindrical Piers. J Hydraulic Eng 137(1):45-56

[9] Nugroho J (2006) Flow Distribution and Scouring around Abutments in Two-Stage Channels. PhD Dissertation, Nanyang Technological University, Singapore

[10] Pu JH (2008) Efficient Finite Volume Numerical Modelling and Experimental Study of 2D Shallow Water Free Surface Turbulent Flows. PhD Dissertation, University of Bradford, Bradford, UK

[11] Liu X, and Garcia MH (2008) Three-Dimensional Numerical Model with Free Water Surface and Mesh Deformation for Local Sediment Scour. J Hydraulic Eng 134(4):203-217

[12] Bihs H, Olsen NRB (2011) Numerical Modeling of Abutment Scour with the Focus on the Incipient Motion on Sloping Beds. J Hydraulic Eng 137(10):1287-1292

[13] Sladkevich M, Militeev AN, Rubin H, Kit E (2000) Simulation of Transport Phenomena in Shallow Aquatic Environment. J Hydraulic Eng 126(2):123-136

[14] Kimura I, Uijttewaal WSJ, Hosoda T, Ali MS (2009) URANS Computations of Shallow Grid Turbulence. J Hydraulic Eng 135(2):118-131

[15] Mahdizadeh H, Stansby PK, Rogers BD (2012) Flood Wave Modeling Based on a Two-Dimensional Modified Wave Propagation Algorithm Coupled to a Full-Pipe Network Solver. J Hydraulic Eng 138(3):247-259

[16] Cao Z, Pender G, Wallis S, Carling P (2004) Computational Dam-Break Hydraulics over Erodible Sediment Bed. J Hydraulic Eng 130(7):689-703

[17] Wu W, Wang SSY (2007) One-Dimensional Modeling of Dam-Break Flow over Movable Beds. J Hydraulic Eng 133(1):48-58

[18] Wu W, Wang SSY (2008) One-Dimensional Explicit Finite-Volume Model for Sediment Transport with Transient Flows over Movable Beds. J Hydraulic Res 46(1):87-98

[19] Xia J, Lin B, Falconer RA, Wang G (2010) Modeling Dam-Break Flows over Mobile Beds using a 2D Coupled Approach. Adv Water Resour 33(2):171-183

[20] Cao Z, Hu P, Pender G (2011) Multiple Time Scales of Fluvial Processes with Bed Load Sediment and Implications for Mathematical Modeling. J Hydraulic Eng 137(3):267-276

[21] Younus M, Chaudhry MH (1994) A Depth-averaged k-ε Turbulence Model for the Computation of Free-Surface Flow. J Hydraulic Res 32(1):415-444

[22] Cea L, Puertas J, Vazquez-Cendon ME (2007) Depth Average Modelling of Turbulent Shallow Water Flow with Wet-Dry Fronts. Arch Comput Method Eng 14(3):303-341

[23] Pu JH, Cheng N-S, Tan SK, Shao S (2012) Source Terms Treatment of SWEs Using Surface Gradient Upwind Method. J Hydraulic Res 50(2):145-153

[24] Ferreira R, Leal J (1998) 1D Mathematical Modelling of the Instantaneous Dam-Break Flood Wave over Mobile Bed: Application of TVD and Flux-Splitting Schemes. Proceedings of European Concerted Action on Dam-Break Modelling, Munich, Germany, 175–222

[25] Yang CT, Greimann BP (1999) Dambreak Unsteady Flow and Sediment Transport. Proceedings of European Concerted Action on Dam-Break Modelling, Zaragoza, Spain, 327–365

[26] Brufau P, Garcia-Navarro P, Ghilardi P, Natale L, Savi F (2000) 1D Mathematical Modelling of Debris Flow. J Hydraulic Res 38(6):435-446

[27] Zhou J, Lin B (1998) One-Dimensional Mathematical Model for Suspended Sediment by Lateral Integration. J Hydraulic Eng 124(7):712-717

[28] Valiani A, Caleffi V (2001) Dam Break Modeling for Sediment Laden Flows. Proceedings of the 2001 International Symposium on Environmental Hydraulics, Arizona, USA, 1-6

[29] Armanini A, Di Silvio G (1988) A One-Dimensional Model for the Transport of Sediment Mixture in Non-Equilibrium Conditions. J Hydraulic Res 26(3):275 – 292

[30] Toro EF (1999) Riemann Solvers and Numerical Methods for Fluid Dynamics: a Practical Introduction. 2nd Edition, Springer-Verlag, Berlin, Germany

[31] Hu K, Mingham CG, Causon DM (2006) A Mesh Patching Method for Finite Volume Modelling of Shallow Water Flow. Int J Num Meth Fluids 50(11):1381-1404

[32] Mingham CG, Causon DM (2000) Calculation of Unsteady Bore Diffraction using a High Resolution Finite Volume Method. J Hydraulic Res 38(1):49-56

[33] Sanders BF, Green CL, Chu AK, Grant SB (2001) Case Study: Modeling Tidal Transport of Urban Runoff in Channels Using the Finite-Volume Method. J Hydraulic Eng 127(10):795-804

[34] Lim SY, Nugroho J (2004) Observations on Flow Field around an Abutment in a Two-Stage Channel. Proceedings of 2nd International Conference on Scour and Erosion, Singapore, 156-164

[35] Melville BW, Chiew YM (1999) Time Scale for Local Scour at Bridge Piers. J Hydraulic Eng 125(1):59-65

[36] Coleman SE, Lauchlan CS, Melville BW (2003) Clear Water Scour Development at Bridge Abutments. J Hydraulic Res 41(5):521-531

List of Table(s):

List of Figure(s):

Table 1. Experimental conditions

No.	Runs	Q_{fm} (l/s)	L (cm)	d_f (cm)	d_m (cm)	d_f/d_m	t_e (hr)	t_{actual} (hr)	d_{se} (cm)	U_f (cm/s)	U_m (cm/s)	Q_{vel} (l/s)
1	20-50-03	50	20	6.40	21.40	0.30	96.0	120	10.0	20.18	27.64	48
2	20-60-02	60	20	3.75	18.75	0.20	27.6	46	10.9	25.77	42.30	57
3	20-60-03	60	20	6.40	21.40	0.30	350.0	503	15.3	24.06	30.73	55
4	20-60-04	60	20	10.00	25.00	0.40	168.0	192	13.2	21.47	24.80	59
5	20-70-03	70	20	6.40	21.40	0.30	53.0	71	18.6	28.26	37.67	66
6	20-70-04	70	20	10.50	25.50	0.41	523.0	546	23.5	22.99	27.12	66
7	35-50-02	50	35	3.75	18.75	0.20	180.0	192	9.9	20.73	36.71	49
8	35-50-03	50	35	6.40	21.40	0.30	115.9	180	15.8	20.18	27.64	48
9	35-50-04	50	35	10.00	25.00	0.40	168.0	174	11.2	17.68	20.63	49
10	35-60-03	60	35	6.40	21.40	0.30	322.0	333	24.1	24.06	30.73	55
11	35-60-04	60	35	10.00	25.00	0.40	174.0	240	19.8	21.47	24.80	59
12	50-50-02	50	50	3.75	18.75	0.20	72.3	78	12.7	20.73	36.71	49
13	50-50-03	50	50	6.40	21.40	0.30	44.0	78.7	15.4	20.18	27.64	48
14	50-50-04	50	50	10.00	25.00	0.40	150.0	168	15.9	17.68	20.63	49
15	50-60-02	60	50	3.75	18.75	0.20	43.0	138	18.5	25.77	42.30	57

Note: All variables and symbols at Table 1 are presented at Nomenclatures section.

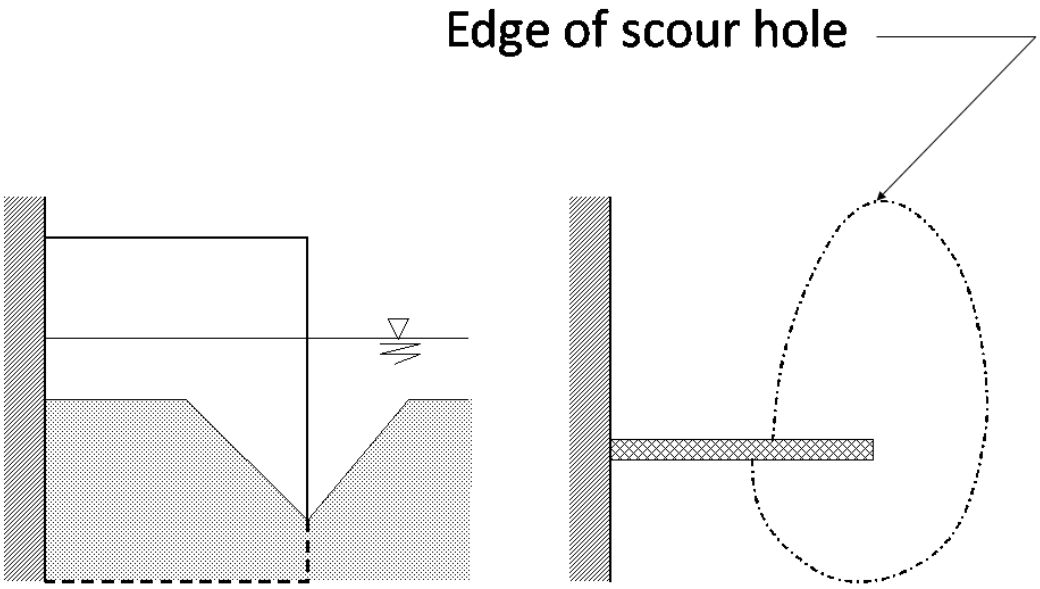

Figure 1(a). Typical cross sectional and plan view of a scour hole

Figure 1(b). Photo example of a scour hole after reaching equilibrium condition (Run 35-50-04)

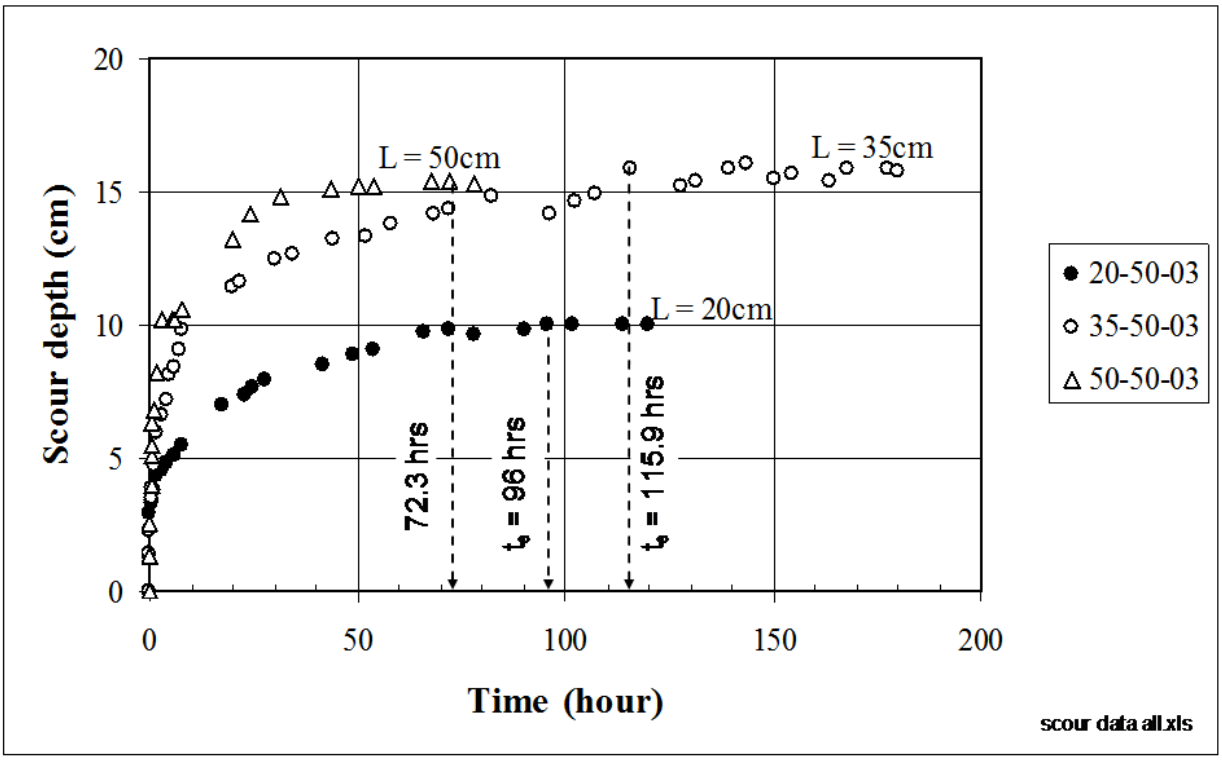

Figure 2. Time development of scour for different abutment lengths under same discharge, Q_{vel} = 48 m^3/s and flow depth ratio, d_f/d_m = 0.3

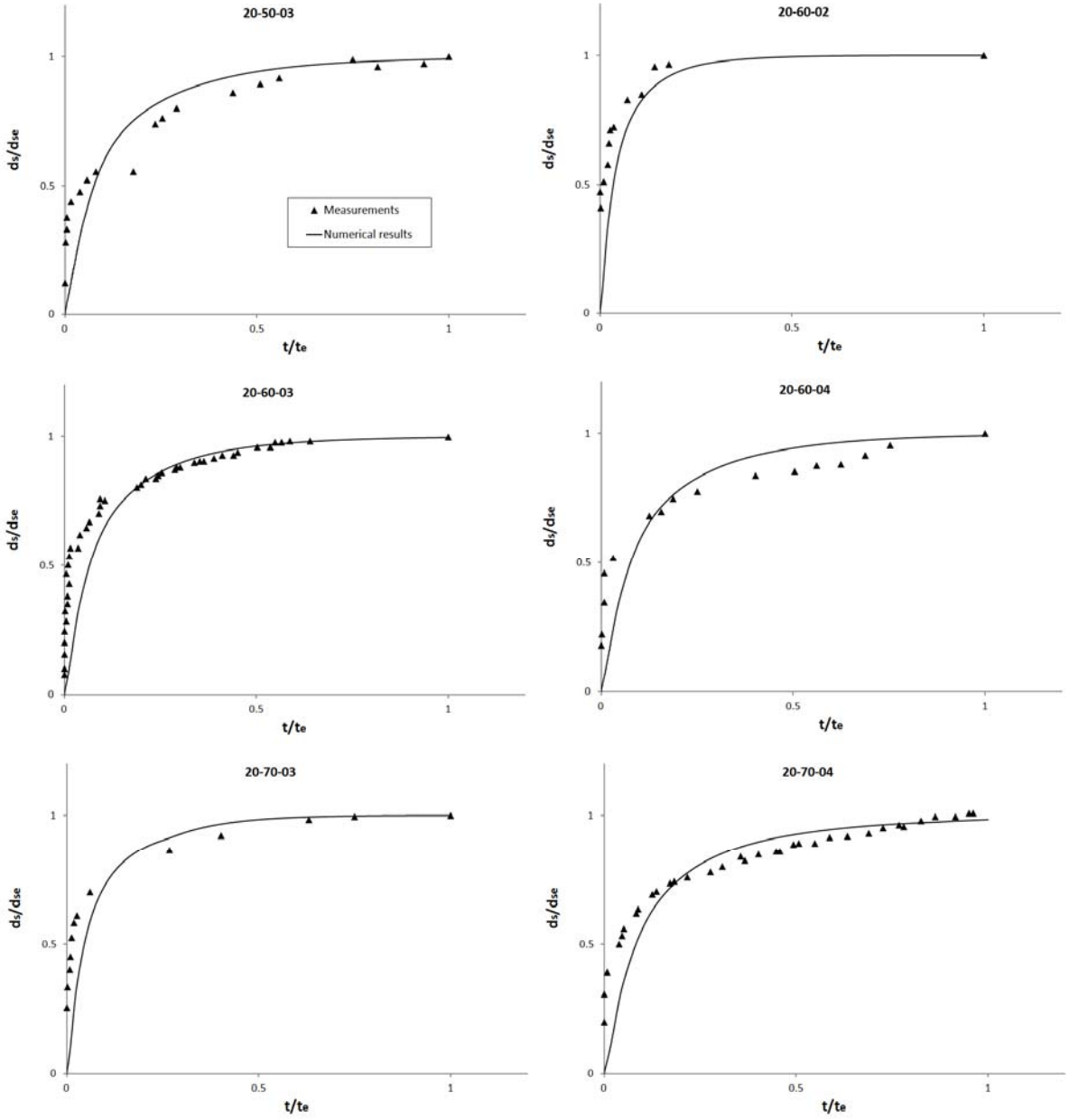

Figure 3. Measured and numerically computed dimensionless scour depth development in experiment with abutment length = 20 cm

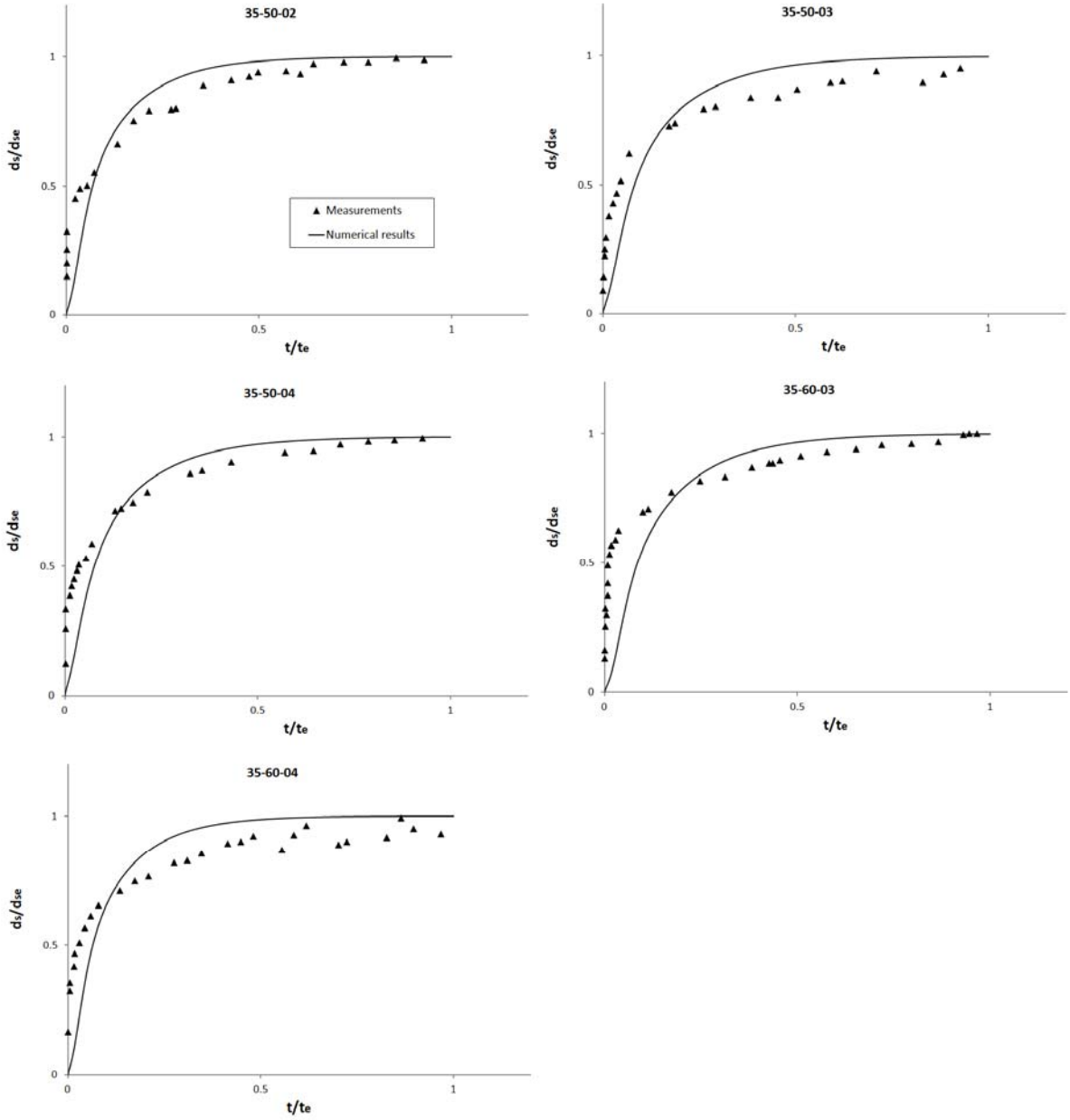

Figure 4. Measured and numerically computed dimensionless scour depth development in experiment with abutment length = 35 cm

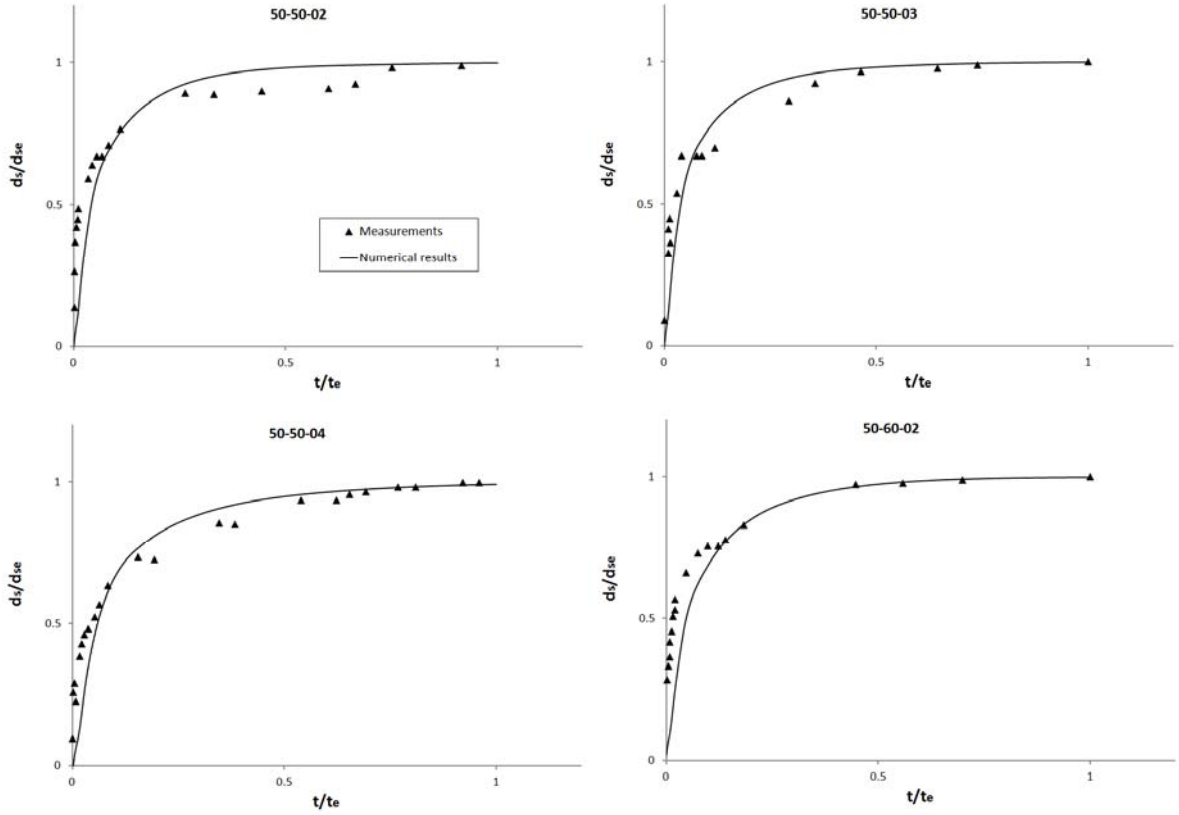

Figure 5. Measured and numerically computed dimensionless scour depth development in experiment with abutment length = 50 cm

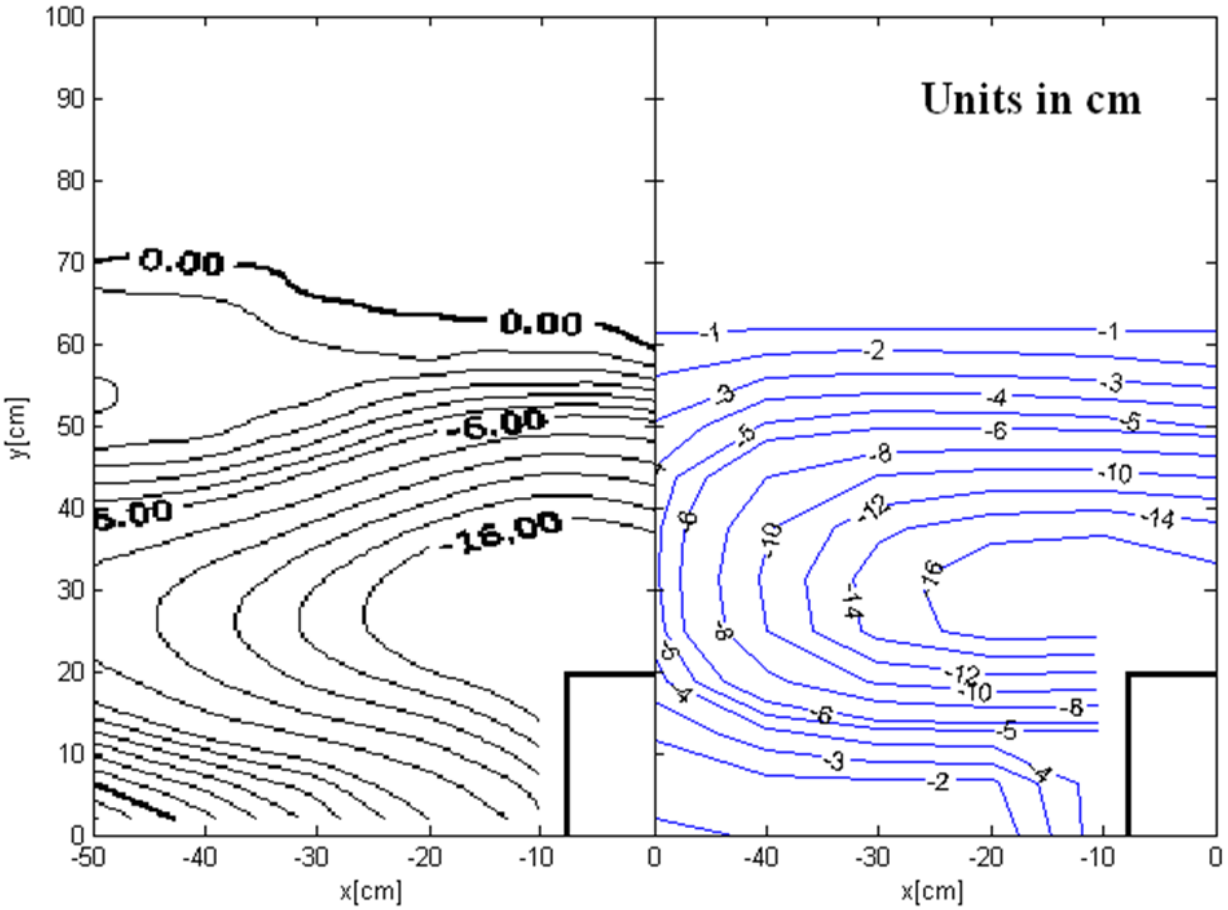

Figure 6. Bed scours comparison of Run 20-70-04 behind the abutment after reaching equilibrium scour of measured data (black-line contours at the left hand side) and numerical simulation (blue-line contours at the right hand side)